

NUMERICAL STUDY ON FLOW AND HEAT TRANSFER PERFORMANCE OF SERPENTINE PARALLEL FLOW CHANNELS IN A HIGH VOLTAGE HEATER SYSTEM

by

Fei DONG*, **Zhiming WANG**, **Yakang FENG**, and **Jie NI**

School of Automotive and Traffic Engineering, Jiangsu University, Zhenjiang, China

Original scientific paper

<https://doi.org/10.2298/TSCI200926168D>

In this study, a high voltage heater system with a size of $310\text{ mm} \times 210\text{ mm} \times 60\text{ mm}$ has been numerically studied and experimentally verified to explore the influence of the cavity structure on the flow and heat transfer performance. The response surface model and analysis of variance are used to determine the influence of the length of the mainstream area of the inlet, L_{in} , the length of the mainstream area of the outlet, L_{out} , the length of the parallel flow channel, L_{ch} , and the single channel width, W , on the flow heat transfer, and ultimately find the best structural plan. The results show that the structural parameters of the parallel flow channel are significantly more important than those of the mainstream area, with the width and length of the parallel single channel being the primary and secondary structural parameters, respectively. The optimization scheme obtained by the NGA-II algorithm can simultaneously meet the requirements of heat transfer and flow uniformity. Specifically, compared with the original model, the flow distribution uniformity coefficient, S , and the inlet/outlet pressure drop, P_{total} , decreased by 53.49% and 19.52%, respectively, while the average heat transfer coefficient increased by 28.05%.

Key words: *high voltage heater system, serpentine parallel flow channels, enhanced heat transfer, structure optimization*

Introduction

In recent years, due to their advantages of high efficiency, simple structure, high driving comfort, and low emissions, electric vehicles have become more and more accepted by people, and have reached a more practical stage. However, the problem of low cruising range in low temperature conditions continues to be one of the main obstacles restricting their development [1-3]. Therefore, under the premise that the heating demand of electric vehicles is guaranteed in a low temperature environment, it is important to reduce the shortening of the cruising range as much as possible for the development and popularization of electric vehicles.

Currently, there are two common heating systems for electric vehicles, namely the positive temperature coefficient (PTC) thermistor heating system and the heat pump heating system. Experimental studies have shown that the PTC heating system can meet the requirements of defogging and defrosting in low temperature environment and heating in winter [4]. However, this heating system has the disadvantage of low efficiency [5, 6]. The heat pump heating system, on the other hand, has obvious advantages in heating efficiency, but its heating efficiency is greatly affected by low temperature. When the ambient temperature is lower than

* Corresponding author, e-mail: jsdxdf@163.com

0 °C, the heat pump heat exchanger is prone to frost formation [7]. Although the heat pump heating system has obvious advantages in heating efficiency, its heating efficiency is greatly affected by low temperature. Accordingly, when the ambient temperature is lower than 0 °C, the heat pump heat exchanger is easily frozen, and the heat pump heating efficiency is reduced [8, 9]. In order to overcome the disadvantages of the PTC heating technology and heat pump heating systems, high voltage heater (HVH) system has become a new choice for electric vehicle heating systems [10], a schematic diagram illustrating an HVH system is shown in fig. 1. On the one hand, compared with the PTC heating technology, the heating efficiency of the HVH system has been significantly improved. On the other hand, compared with the heat pump heating technology, at an ambient temperature of -45 to +70 °C, the high power output of the HVH system can also be maintained.

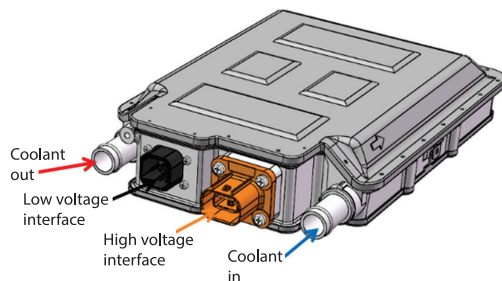


Figure 1. Schematic diagram of the high voltage electric heating system

worth noting that such uneven flow distribution will ultimately have a great impact on the performance of the equipment [14-17]. Therefore, it is necessary to investigate the influence of the cavity structure parameters on the heat and mass transfer characteristics of the high voltage electric heating system to improve its working performance.

Many studies have been conducted on the influence of the flow channel structure parameters on the flow characteristics of the fluid in the flow channel and the design of a flow channel structure with more uniform flow distribution [18-20]. Maharudrayya *et al.* [21] designed seven flow channel structures by CFD simulation, optimized the original model using the uniformity of the flow distribution and pressure drop as evaluation indicators. Their results showed that the parallel flow channel can significantly improve the uniformity of the flow distribution through the control of the pressure drop by improving the structural parameters. Huang *et al.* [22] performed theoretical calculations and CFD simulations on single-layer and multi-layer parallel flow channels with the same structure. They found that the flow channel structure has a great influence on the flow characteristics of the fluid, which is consistent with the finding of [21]. Liu *et al.* [23, 24] studied the heat transfer and flow performance of the new T and T-Y micro-channel heat sinks with liquid GaInSn coolant. They found that both structures have excellent heat transfer and temperature-evenness performances. Biswal *et al.* [25] studied the heat and mass transfer characteristics of a rectangular radiator with parallel flow channel structure through experiments and CFD simulation calculation methods, and analyzed the influence of parameters, such as flow channel aspect ratio, radiator substrate thickness, material, inlet flow rate, etc., on the thermal resistance and pressure drop of the radiator. Wang [26, 27] performed calculations using CFD simulations on the flow and pressure distribution in the U-shaped and Z-shaped parallel flow channels in the fuel cell stack, and proposed a design optimization method for parallel flow channels based on the results of the simulation of multiple

The interior of the heat exchanger cavity of the HVH system is a parallel serpentine flow channel structure, which has the advantages of compact structure and large heat exchange area. It is widely used in various devices such as microelectronic radiators and lithium battery cooling systems [11-13]. However, studies have found that uneven flow distribution usually occurs in parallel flow channels. The degree of uneven flow distribution is mainly determined by structural parameters, such as the shape and size of the flow channel. It is

flow conditions and flow channel structure parameter combination schemes. Tong *et al.* [28] designed and calculated a variety of parallel flow channel structure schemes using CFD simulation calculation methods, compared the advantages and disadvantages of each scheme using the exit flow of each subchannel as the evaluation index. They ultimately obtained the rule for the influence of multiple channel structure parameters on the uniformity of the flow distribution.

However, few studies on HVH systems have been reported and there is hardly published research on serpentine parallel flow channels in HVH systems. Therefore, according to the aforementioned research status, it is valuable and necessary to investigate serpentine parallel flow channels in HVH systems to enhance the stability and heat transfer capacity of such energy-efficient heating systems.

The main objectives and procedures performed in this study can be summarized as follows. The simulation is carried out on the existing HVH system, and the model accuracy is verified by heat transfer performance experiments. The approximate model of the cavity mainstream area-parallel flow channel structure in the HVH system is established by the response surface method. Also, the influence of multiple structural parameters on the evaluation index of the flow heat transfer characteristics of the heater is determined. In addition, the contribution rate of each parameter to the evaluation index of the flow heat transfer characteristics was analyzed by analysis of variance (ANOVA), and the optimization scheme was implemented using the NGS-II algorithm.

Numerical analysis

Original geometry model

The existing HVH systems, excluding the upper and lower shell models, are defined as the simulation domain. The structure of the geometric model of the HVH system is shown in fig. 2. Specifically, an HVH system with a total size of $310 \text{ mm} \times 210 \text{ mm} \times 60 \text{ mm}$ is shown in fig. 2(a), and the geometric model of the parallel flow channel area in the duct is shown in fig. 2(b).

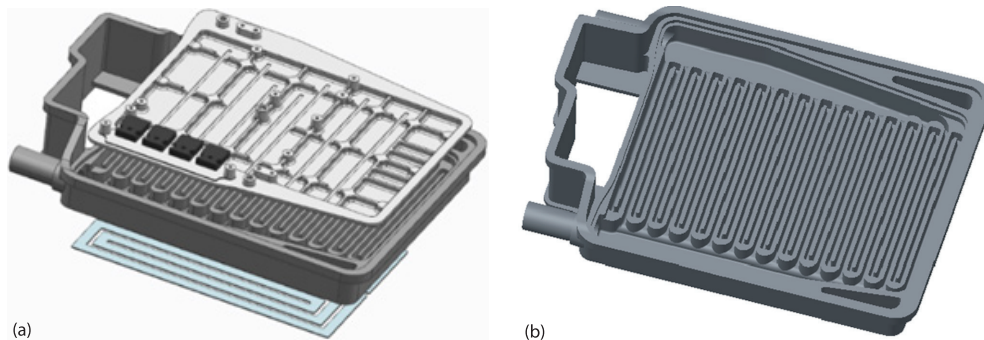


Figure 2. The 3-D structure of the geometric model of the high voltage heating system; (a) overall structure diagram [11] and (b) mainstream area-parallel flow path

Governing equations

This paper assumes that the heat exchange medium is an incompressible steady-state fluid in 3-D. Then, the Reynolds number of the heat exchange medium at the inlet of the heat exchanger is calculated to be 11948.9 higher than 2300, and it is finally confirmed that it is turbulent. Therefore, the heat exchange medium should follow the three basic conservation laws,

namely conservation of mass, conservation of momentum and conservation of energy. In this paper, the Euler method is used to describe the motion form of the fluid particle in the flow field. The three equations are:

– Continuity equation

$$\frac{\partial}{\partial x_i}(\rho u_i) = 0 \quad (1)$$

– Momentum equation

$$\frac{\partial(\rho u_j)}{\partial x_j} = -\frac{\partial p}{\partial x_i} + \frac{\partial}{\partial x_i} \left(\mu \frac{\partial u_j}{\partial x_i} \right) \quad (2)$$

– Energy equation:

$$\frac{\partial}{\partial x_i} \left(\lambda \frac{\partial T}{\partial x_i} \right) = \nabla(\lambda \nabla T) \quad (3)$$

Here, the SST $k-\omega$ model is used to calculate the flow field and temperature field inside the heat exchanger. The SST $k-\omega$ model combines the advantages of the $k-\omega$ model in the near-wall region and those of the $k-\omega$ model in the far field, and can obtain a high resolution in the near-wall flow solution that is more in line with the physical situation [29], the transport equation of the turbulent kinetic energy, k , and specific dissipation rate, ω , can be expressed:

$$\frac{\partial}{\partial x_j}(\rho k u_j) = \frac{\partial}{\partial x_j} \left[(\mu + \sigma_k \mu_t) \frac{\partial k}{\partial x_j} \right] + \tau_{ij} \frac{\partial u_i}{\partial x_j} - \beta^* \rho \omega k \quad (4)$$

$$\frac{\partial}{\partial x_j}(\rho \omega u_j) = \frac{\partial}{\partial x_j} \left[(\mu + \sigma_\omega \mu_t) \frac{\partial \omega}{\partial x_j} \right] + \frac{\gamma}{v_t} \tau_{ij} \frac{\partial u_i}{\partial x_j} - \beta \rho \omega^2 + 2(1 - F_1) \rho \sigma_{\omega 2} \frac{1}{\omega} \frac{\partial k}{\partial x_j} \frac{\partial \omega}{\partial x_j} \quad (5)$$

where ρ is the density and μ is the dynamic viscosity,

$$v_t = \frac{\rho \alpha_1 k}{\max(\alpha_1 \omega, \Omega F_2)} \text{ is the eddy viscosity coefficient}$$

Ω is the vorticity, and

$$F_2 = \tanh \left[\max \left(2 \frac{\sqrt{k}}{0.09 \omega y}, \frac{500 v}{y^2 \omega} \right)^2 \right]$$

where F_1, F_2 are compound functions, $\tau_{ij} = -\rho \overline{u'_i u'_j}$ – the Reynolds stress, $\tau_{ij}(\partial u_i / \partial x_j)$ – the generation term of the turbulent kinetic energy, $\alpha_1 = 0.31$, $\beta^* = 0.09$, $\beta = 0.075$, and $k = 0.41$.

In this paper, a second-order upwind scheme are used to solve momentum, energy and $k-\omega$ equation, and SIMPLEC algorithm is used to solve pressure-velocity coupling.

Boundary conditions

The numerical simulation was developed using the commercial CFD software SC/Tetra V13 (MSC/Cradle, Osaka, Japan). Accordingly, the actual condition of the heating performance test of the high voltage electric heating system at a rated power of 5 kW is used as the boundary condition for numerical simulation. The flow boundary conditions are set the inlet flow rate is 700 lph, the inlet temperature is 73.96 °C, and the outlet relative static pressure is 0 Pa.

The setting of the thermal boundary conditions can be summarized as follows. The heating element power is set to 5 kW, since the heat exchanger is in direct contact with the external environment, there is natural-convection heat exchange with the air, so the natural-convection heat transfer coefficient (HTC) of the heat exchanger outer wall is set to 5 W/m²K. The fluid-solid coupling interface is composed of the heat exchanger cavity cover and the inner wall surface of the cavity, which achieves data exchange between the fluid and solid during the numerical simulation, so its type is defined as interface. The detailed schematic diagram of the calculation model with boundaries is shown in fig. 3.

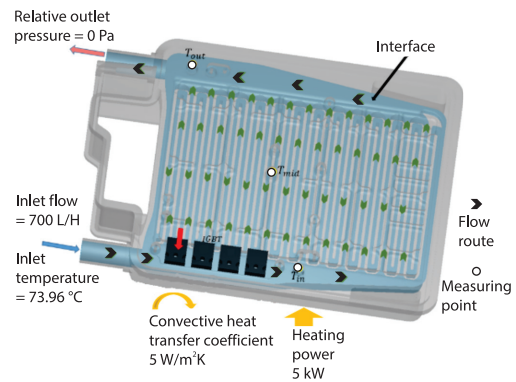


Figure 3. Numerical calculation model diagram of HVH system with boundary conditions

Graphene nanofluid is used as the heat transfer medium and its main physical parameters when the temperature is 73.96 °C are shown in tab. 1. The thermal conductivity of graphene/propylene glycol nanofluids is tested using the Hot Disk TPS-500S thermal constants analyzer (Hot Disk AB), a Changji NDJ-5S inner cylinder rotational viscometer (Shanghai Changji Geological Instrument Co., Ltd.) was used to test viscosity, Xiangke (BRR-3C) specific heat capacity measuring instrument was used to test Specific heat capacity.

Table 1. Thermophysical parameters of graphene nanofluid

Material	ρ [kgs ⁻¹]	C_p [Jkg ⁻¹ K ⁻¹]	κ_p [Wm ⁻² k ⁻¹]	μ [Pa·s]
Graphene nanofluid	1013.15	3.56	0.398	1.31

Grid independence

The best grid scheme to ensure the accuracy of the simulation calculations and save the computing resources of different grid schemes is found by verifying the grid independence. The inlet temperature, T_{in} , intermediate runner temperature, T_{mid} , output temperature, T_{out} , and inlet and outlet pressure drop, P_{total} , in different grid schemes are recorded, and the specific temperature measurement place is shown in fig. 3. Then, the temperature of these measuring points and the size of the pressure drop at the inlet and outlet are used as grid-independent evaluation indexes, and the changes of each evaluation index value with the basic grid size are compared. The total numbers of mesh of solid and fluid domains and calculation results of the grid-independent indicators in different grid types are shown in tab. 2. Comparing grid Types 5 and 6, the errors of the temperature of each measurement point are 0.23%,

Table 2. Grid independence calculation results

Mesh type	Number of mesh	T_{in} [°C]	T_{mid} [°C]	T_{out} [°C]	P_{total} [Pa]	Y^+
1	863632	79.34	99.82	86.97	3688.57	1.35
2	1434845	80.19	100.31	86.05	3667.09	1.23
3	1985960	80.70	101.64	85.24	3656.28	1.12
4	2465816	81.27	102.28	84.68	3645.19	1.10
5	2969177	81.68	102.79	84.20	3634.04	1.05
6	3432218	81.87	102.98	84.06	3626.03	1.02

0.19%, and 0.17%, respectively, and the error of the pressure drop is 0.22%. The error is the smallest among Schemes 1-6. These results indicate that when the body grid is less than 1.2 mm, the simulation results are independent of the body grid size. Therefore, after weighing the calculation accuracy and calculation cost, the grid Scheme 5 with a basic grid size of 1.2 mm was selected as the grid scheme for the simulation calculations of the high voltage electric heating system. The grid model of the cavity structure and fluid domain of the high voltage heating system is shown in fig. 4.

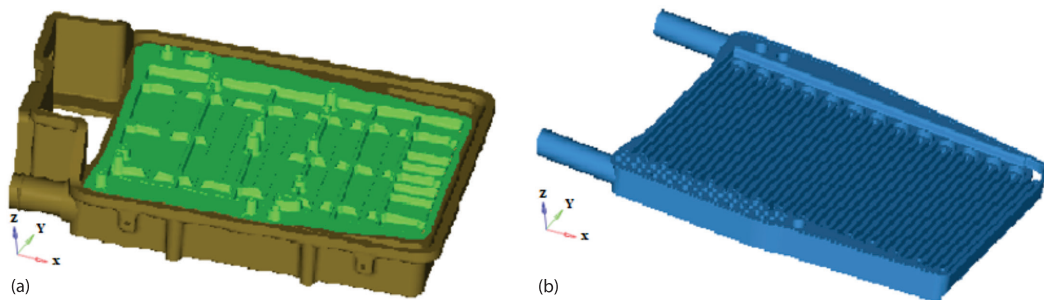


Figure 4. Mesh model of the cavity structure in high voltage electric heating system; (a) solid domain and (b) fluid domain

Model verification

In order to ensure the accuracy of the simulation results and that the analysis based on the simulation results is reasonable and credible, the simulation results and their corresponding test results are compared and verified. The diagram of the HVH system experimental used in this study is shown in fig. 5. The measured point temperatures T_{in} , T_{mid} , T_{out} , and P_{total} are still used as evaluation indicators for the verification of the accuracy of the simulation results. The simulation results, test results and their errors for each evaluation index are shown in tab. 3. The maximum error occurs at the temperature measuring point T_{in} , which is 2.13%, and the errors of the remaining evaluation indexes are within 1.6%. The simulation and test results show good agreement. Therefore, the simulation model established in this paper is highly accurate.

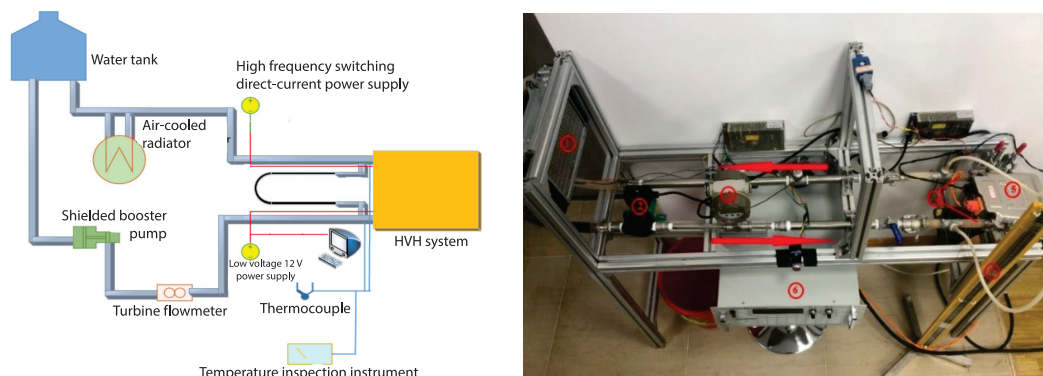


Figure 5. Diagram of the heating test bench for the HVH system; 1 – radiator, 2 – shielded booster pump, 3 – turbine flowmeter, 4 – dual-channel K-type thermocouple, 5 – HVH system, 6 – temperature monitor instrument, and 7 – U-shaped manometer

Table 3. Comparison of the simulation results and test results

Comparison parameters	T_{in} [°C]	T_{mid} [°C]	T_{out} [°C]	P_{total} [Pa]
Simulation results	81.68	102.79	84.2	3634.04
Test results	83.46	101.66	85.53	3597.12
Relative error [%]	2.13	0.85	1.56	1.03

Experimental scheme

As shown in fig. 6, the length of the mainstream area of the inlet, L_{in} , the length of the mainstream area of the outlet, L_{out} , the length of the parallel flow channel, L_{ch} , and the single channel width, W , are selected as variables for multi-objective optimization. The L_{ch} is the maximum distance between the two top ends of the flow channel, and W is the width of a single flow channel in a single serpentine sub-flow channel. A single serpentine subchannel containing three single channels is shown in red in fig. 6. Since the reserved position of the HVH system installed in a real vehicle is relatively fixed, when designing the sample scheme, the range of values of the optimized variables is based on not changing the outer edge of the inner wall surface of the existing heat exchanger cavity. The total length, L_{total} , inside the heat exchanger cavity in the inlet direction is 209 mm. As indicated by the yellow mark in fig. 6, the single channel wall thickness of the serpentine subchannel is 2.2 mm and fixed. The number of flow channels is negatively related to W . After W is determined, the number of flow channels is obtained by a trial and error approach. Schematic diagram of the flow path marked in red. Finally, based on the aforementioned idea of selecting the range of optimization variables, the upper and lower limits of each optimization variable ultimately determined are shown in tab. 4.

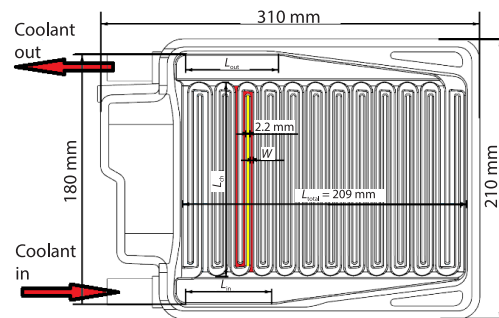


Figure 6. Schematic diagram of structural parameters and optimization variables of the cavity

Table 4. Range of the design optimization variable

Factors	Lower value	Upper value
L_{in} [mm]	56	91
L_{out} [mm]	55	76
L_{ch} [mm]	114	142
W [mm]	2.8	5.6

Design of sample

In this paper, the sample schemes for different optimization variables are designed by the Latin hypercube sampling method [30]. The number of sampling points needs to satisfy:

$$N \geq \frac{(M+1)(M+2)}{2} \quad (6)$$

where N is the minimum number of sample points required and M – the number of optimization variables.

Using this sampling method, a higher sampling accuracy can be obtained with a smaller sampling scale, which has the great advantage of giving a high precision approximate model response for a given space [30]. The simulation results of the 15 sample schemes designed and the optimization goals corresponding to each scheme are shown in tab. 5. The sample standard deviation of the flow at the entrance of each flow channel is defined as the flow distribution uniformity coefficient, S . The S is used to evaluate the unevenness of the flow distribution. The smaller the value of S , the more uniform the flow distribution, which is calculated:

$$S = \sqrt{\frac{1}{N-1} \sum_{i=1}^{13} (q_i - \bar{q})^2} \quad (7)$$

where q_i is the flow rate in the i^{th} flow channel and \bar{q} [10^{-4} s^{-1}] is the average flow rate of all flow channels.

Table 5. Design of the sample schemes and results of the optimization objective

Test	Test factors				Test results		
	L_{in} [mm]	L_{out} [mm]	L_{ch} [mm]	W [mm]	P_{total} [Pa]	S	HTC [$\text{Wm}^{-2}\text{K}^{-1}$]
1	91	62.5	134	4.8	2594.5	34.7	3462.5
2	56	59.5	130	4.2	2821.2	35.6	3890.2
3	73.5	55	126	5.2	2566.2	68.5	3674.9
4	63.5	68.5	142	3.4	3529.9	54.7	3795.2
5	86	67	132	2.8	4153.9	20.5	3501.2
6	83.5	74.5	118	3.8	2909.3	33.4	3893.1
7	58.5	73	128	5	2525.4	59.9	3728.5
8	88.5	61	116	4	2698.3	41.6	3583.7
9	71	58	120	3	3255.1	38.9	3481.9
10	61	71.5	124	3.2	3346.4	47.2	3866.7
11	76	56.5	138	3.6	2981.4	54.1	3933.6
12	81	70	122	5.6	2148.3	61.9	3570.9
13	78.5	76	136	4.4	2848.2	29.9	3747.8
14	68.5	64	140	5.4	2682.4	71.5	3708.6
15	66	65.5	114	4.6	2396.8	43.7	3595.1

Establishment of approximate model of the response surface

The response surface analysis method [31] is used as a proxy method, and the multivariate quadratic response surface approximate model formula for each optimization goal is:

$$\eta = \beta_0 + \sum_{j=1}^M \beta_j X_j + \sum_{j=1}^M \beta_{jj} X_j^2 + \sum_{i < j} \sum_{j=2}^M \beta_{ij} X_i X_j + \varepsilon_0 \quad (8)$$

where η is the predicted value of the response surface, X_j , X_j^2 and the variable value after X_i encoding, β_0 – the regression constant, β_j , β_{jj} , and β_{ij} are the linear coefficient, co-ordination coefficient, and square coefficient, respectively, M – the optimization number of variables, and ε_0 – the random error.

The data in tab. 6 shows that the errors between the optimization target values obtained by the simulation calculation and response surface analysis are small, and the coefficient of determination R^2 is very close to 1. Therefore, the established response surface model can more accurately reflect the influence of optimization variables on optimization goals.

Table 6. Evaluation of the accuracy of the response surface model

Response results	Average error	Maximum error	R^2
S	2.14	3.18	0.9799
P_{total} [Pa]	2.52	3.21	0.9726
HTC [$\text{Wm}^{-2}\text{K}^{-1}$]	0.47	1.62	0.9935

Results and discussion

The influence of mainstream zone parameters on optimization variables

The effects of the L_{in} and L_{out} on the S , P_{total} , and HTC , when the L_{ch} is 138 mm and W is 4.2 mm, are shown in figs. 7-9.

The influence of the mainstream parameters on S

As shown in fig. 7(a), the S value shows a downward trend with the increase of the L_{in} and L_{out} . At the maximum value of both L_{in} and L_{out} , S has a minimum value of 9.6. Taking the middle value of L_{out} and L_{in} ($L_{\text{out}} = 65.5$ mm and $L_{\text{in}} = 73.5$ mm) as the research object. The change trend of the S with the L_{in} alone can be determined, when the L_{out} is 65.5 mm in fig. 7, using the curve of the S with the L_{in} shown in fig. 7(b). With the increase of the L_{in} , the S shows a monotonous decreasing trend, and the flow rate of the rear flow channel increased with the increase of the L_{in} . Since the increase of the L_{in} weakens the diversion effect of the front and middle flow channels, and the space near the entrance of the rear flow channel is large, the uniformity of the flow distribution is improved. However, when the L_{in} is 73.5 mm, the S shows a decreasing trend at first and then an increasing trend, as shown in the variation curve of the S with L_{out} in fig. 7(c). The uniformity of the flow distribution is not optimal when its length reaches the maximum or minimum value. When searching for the law of influence on the S , the influence of the coupling between the L_{out} and L_{in} on the S should be considered. The data shown in fig. 7(a) reveals that at the minimum L_{in} value and the maximum L_{out} value, the S reaches its maximum value of 56.59. Since the coupling effect of the L_{in} and L_{out} is the worst in this structural scheme, at the minimum L_{in} value, the space near the inlet of the rear channel is narrow, and it is difficult for the heat transfer medium to enter the channel, resulting in a small flow rate. At the same time, at the maximum L_{out} value, the oblique angle of the rear oblique flow channel reaches the maximum angle, which fully satisfies the space requirements of the rear flow channel for outflow. As a result, after the heat exchange medium flows out from the outlet of the flow channel, the pressure increases, and the flow velocity decreases due to the sudden increase in the flow area. Similarly, at the maximum L_{in} value and minimum L_{out} value, the S value (47.23) is also high due to the length mismatch between the L_{in} and L_{out} . Therefore, when studying the uniformity of the flow distribution, the coupling of the L_{in} and L_{out} should be fully considered.

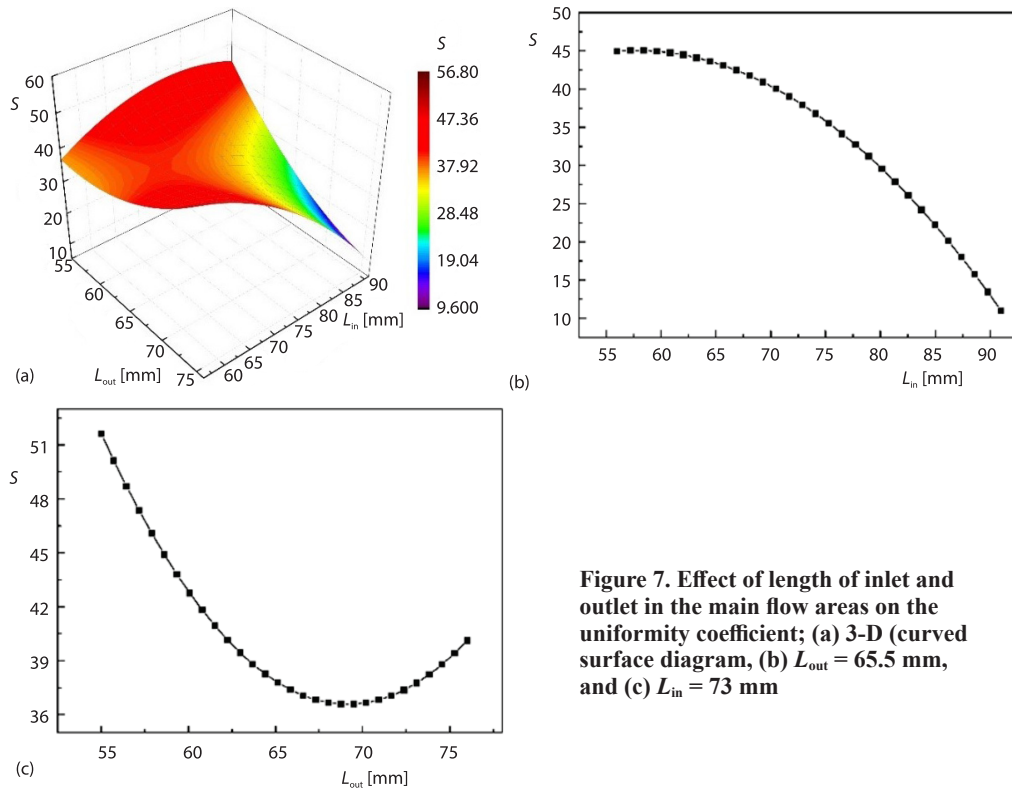


Figure 7. Effect of length of inlet and outlet in the main flow areas on the uniformity coefficient; (a) 3-D (curved surface diagram, (b) $L_{out} = 65.5$ mm, and (c) $L_{in} = 73$ mm

The influence of mainstream parameters on the P_{total}

The illustration of the influence of the L_{in} and L_{out} on the P_{total} shown in fig. 8(a) reveals that with the increase of the L_{in} , the P_{total} decreases at first and then increases. Since the L_{in} value is too small, the length of the oblique flow channel in the inlet mainstream area is relatively large, and the increase in the length of the flow channel results in more loss of flow resistance. Moreover, when the L_{in} value is small, the degree of narrowing of the overflow area in the main flow area of the rear flow channel is increased. As a result, the heat exchange medium can maintain a relatively high flow rate when flowing to the rear flow channel. However, since the space near the entrance of the rear flow channel is too narrow, the heat exchange medium has a greater local resistance loss due to the higher flow rate and the rapid change of the flow direction.

The P_{total} clearly moderately increases with the increase of the L_{out} . When the L_{out} increases, the length of the oblique flow channel in the main flow area of the outlet is shortened, and the space near the outlet of the rear flow channel is increased, so that the structure of the outlet of the rear channel drastically changes, the internal friction of the fluid and the loss of local resistance are increased.

Considering the effect of the coupling of the L_{in} and L_{out} on the P_{total} , the degree of increase of the P_{total} due to the increase of the L_{out} with the increase of the L_{in} . The 2-D contour of the P_{total} with the L_{in} and L_{out} is shown in fig. 8(b). The gradient of the P_{total} along the positive direction of the L_{out} becomes larger as the L_{in} becomes larger. Due to the increase of the L_{in} , the flow in the rear flow channel increases, which leads the formation of vortices at the outlet of the flow channel to be strengthened. Likewise, the effect of the outlet oblique flow channel on the

suppression of vortex formation is increased. Simultaneously, the change of the P_{total} due to the increase of the L_{out} is larger than that with a smaller L_{in} value.

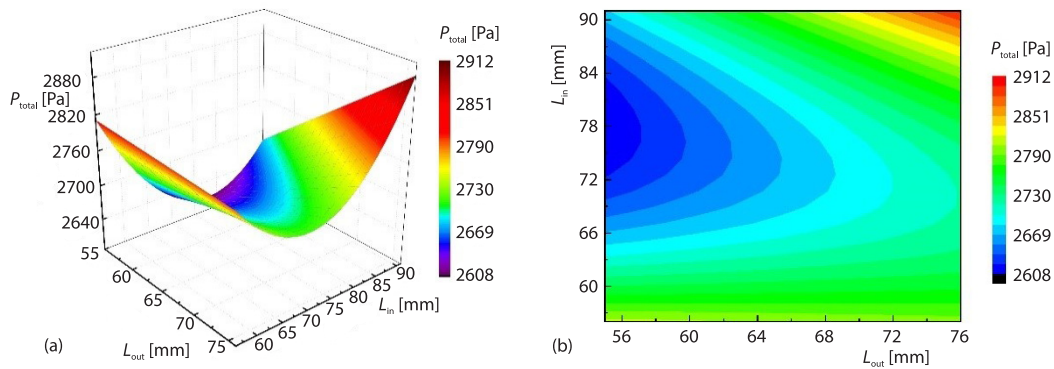


Figure 8. Effect of the length of the inlet and outlet main flow areas on the pressure drop; (a) 3-D curved surface diagram and (b) 2-D isogram diagram

The influence of mainstream parameters on the HTC

As shown in fig. 9(a), the average HTC with the L_{in} and L_{out} both show an increasing trend at first and then a decreasing trend. At the same time, as shown in fig. 9(b), when the HTC value is larger, the L_{in} value is 67.9~84.5 mm, and the L_{out} value is 61.3~73.6 mm. According with the results shown in fig. 7, in the aforementioned value ranges of L_{in} and L_{out} , the S value is relatively small, which indicates that the S has an important influence on the HTC. Since, under the same conditions, the HTC is determined by various factors, such as the physical properties of the fluid, the flow rate, the thermal conductivity of the material, and the solid structure, the average flow rate in the heat exchanger cavity plays a decisive role in the size of the average HTC value. However, the L_{in} and L_{out} values at the maximum HTC value do not completely correspond to the values at the minimum S value. At the minimum S value, the values of L_{in} and L_{out} are both upper limit values, and the flow area of the main flow area at both ends of the inlet and outlet is the largest among all schemes. Thus, when the inlet flow rate is fixed, the average velocity of the fluid decreases with the increase of the flow area, so the average HTC decreases. From the perspective of the effect of the coupling effect of the L_{in} and L_{out} values on the HTC,

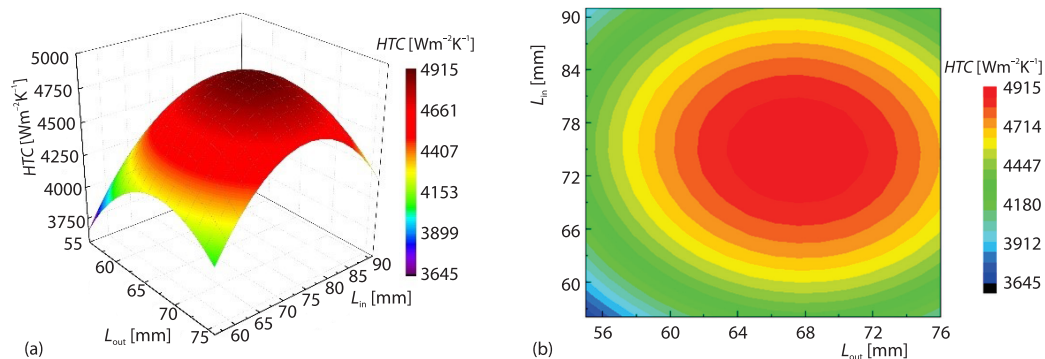


Figure 9. Effect of the length of the inlet and outlet main flow areas on the HTC; (a) 3-D curved surface diagram and (b) 2-D isogram diagram

the HTC value is smaller at the upper and lower limit values of the L_{in} and L_{out} . However, the corresponding S value is relatively high. Which indicates that the mismatch of the L_{in} and L_{out} values deteriorates the overall flow characteristics in the heat exchanger cavity and reduces the heat exchange capacity of the heat exchanger.

Influence of the flow channel parameters on the optimization variables

The effects of the W and L_{ch} on the S , P_{total} , and HTC when the L_{in} is 73.5 mm and L_{out} is 65.5 mm, are shown in figs. 10-12.

The influence of the flow channel parameters on the S

As shown in fig. 10(a), the S shows a gradual increasing trend with the increase of the width W of the unidirectional flow channel. However, in the process of increasing the W from 2.8-3.2 mm, the change of the S is not obvious. When the W increases from 3.2-5.6 mm, the increase of the S is quite significant. The reason for this phenomenon is that the W value is inversely proportional to the number of flow channels. When the W increases from

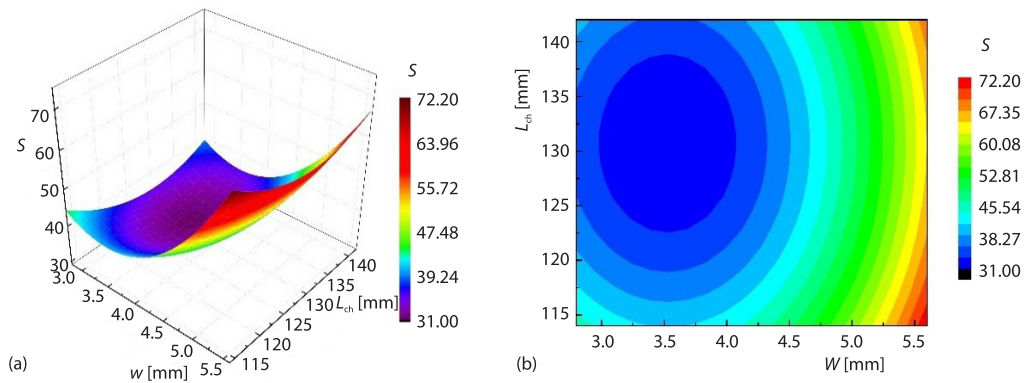


Figure 10. Effect of the parallel channel length and single channel width on S ;
(a) 3-D curved surface diagram and (b) 2-D isogram diagram

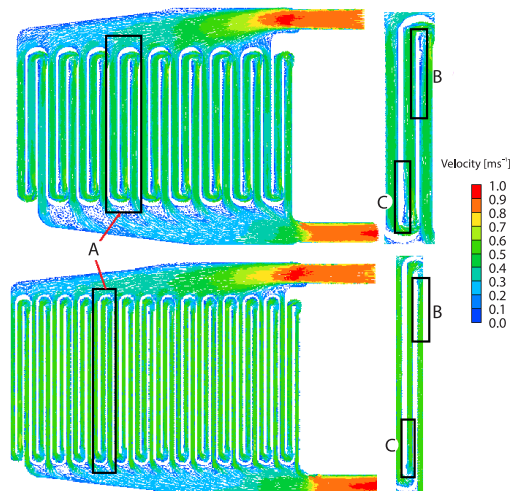


Figure 11. Diagram of velocity distribution for different channel numbers

2.8-3.8 mm, the number of flow channels decreases by 7.69%, but when the W increases from 3.8-5.6mm, the number of channels is reduced by 25%. The results of the experimental research on the uniformity of the flow distribution of parallel flow channels were obtained from a previous study [32], which revealed that the increase in the number of flow channels is conducive to the improvement of the uniformity of the flow distribution. As shown in fig.11, when the number of channels increases from 9 to 14, the flow velocity in all areas increases. However, taking a single Channel A as an example, in areas B and C, the uniformity of the velocity distribution with the number of channels, 9, is lower than that with the number of channels, 14. At the same time, with the parallel flow channel length L_{ch} , the S shows a decreasing trend at first and then an increasing trend. Also, the change in the L_{ch} value changes the width of the entrance and exit of the mainstream area. Taking the effect of L_{ch} on the width of the entrance mainstream area as an example, when the L_{ch} value is too large, the width of the entrance mainstream area is narrow, and the space near the entrance of the rear flow channel is narrow, which obviously increases the difficulty of the flow of the heat exchange medium into the rear flow channel. When the L_{ch} value is too small, the flow area of the inlet main flow area increases significantly. After the fluid enters the water inlet, the flow rate decreases and the pressure increases, so that the inlet pressure of the front and middle flow channels also increases, which affects the flow rate. The increase of the inlet pressure of the front and middle flow channels is conducive to the increase of its own flow rate, which strengthens the diversion effect of the front and middle flow channels. However, it is not conducive to the uniformity of the flow distribution. Therefore, choosing a moderate L_{ch} value will lead to a smaller S value. In addition, fig. 10(b) shows that the gradient distribution of the S along the positive direction of the W is much greater than the L_{ch} , and the influence of the W on the S is significantly greater than that of the L_{ch} .

The influence of the flow channel parameters on the P_{total}

As shown in fig. 12(a), the P_{total} shows a monotonous increasing trend with the increase of the L_{ch} . According to the Darcy formula, the longer the flow channel length, the greater the resistance loss along the flow. The Darcy formula is shown:

$$h_f = \lambda \frac{l}{d} \frac{v^2}{2g} \tag{9}$$

where λ is the coefficient of friction, l is the length of the flow channel, d is the width of the runner, which is proportional to the W , v is the flow rate, and g is the acceleration of gravity.

The P_{total} shows a monotonous decreasing trend with the increase of the W . There are three reasons for this phenomenon. First, according to the Darcy formula, with the increase in the W , the resistance loss in the single channel will decrease. Second, the increase in the W reduces the number of flow channels, which more markedly reduces the total flow resistance loss along the length of the flow channels. Third, the increase in the W facilitates the entry of the fluid into flow channel, which reduces the local pressure loss of the fluid at the inlet corner.

As shown in fig. 12(b), the P_{total} gradient in the positive direction of the W is relatively large. Taking the parallel flow channel length as 76 mm as an example, when the W is 2.8 mm, the P_{total} is 4209.96 Pa, but when the W is 5.6 mm, the P_{total} is 2633.76 Pa, a decrease of 37.46%. The P_{total} gradient in the positive direction of the W is much larger than that in the positive direction of the L_{ch} , which indicates that the W has a more significant effect on the P_{total} than that of the L_{ch} . To summarize, according to figs. 10(b) and 12(b), properly increasing the width of the single channel can have a better effect on reducing the pressure drop at the inlet and outlet without significantly deteriorating the uniformity of the flow distribution.

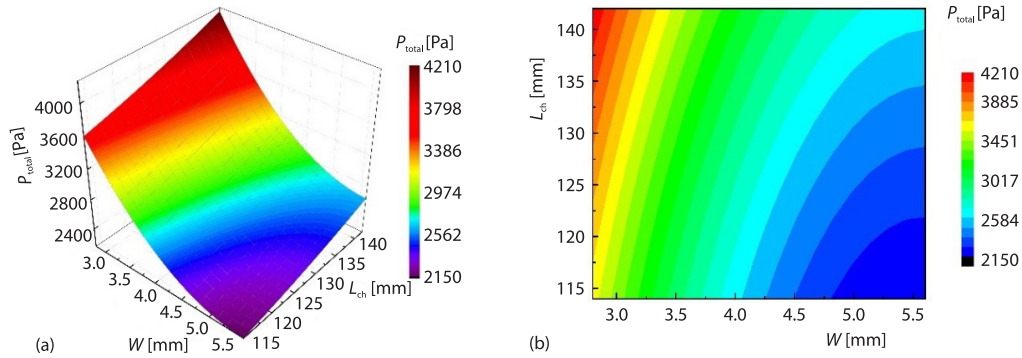


Figure 12. Effect of the parallel channel length and single channel width on the pressure drop; (a) 3-D curved surface diagram and (b) 2-D isogram diagram

The influence of the flow channel parameters on the HTC

As shown in fig. 13(a), with the increase of L_{ch} , the HTC increases at first and then decreases, and the same trend is observed with the change of the W of the single channel. The range of the L_{ch} and W values when the HTC has a larger value in fig. 13(b) is almost the same as the range of the L_{ch} and W values when the S has a smaller value in fig. 10(b). These findings are also consistent with the previous findings after analyzing the correlation between the S and HTC with L_{in} and L_{out} as variables. They once again verify that the improvement of the uniformity of the flow distribution is beneficial to the enhancement of the heat exchange capacity of the heat exchanger. However, a comparison of the results in figs. 13(b) and 10(b) revealed that the range of W when HTC has a large value is slightly larger than the range value of W when S has a small value. The flow characteristics of the heat exchange medium will improve with the increase of the W value. Therefore, after ensuring a good uniformity of the flow distribution, the average HTC in the heat exchanger cavity is increased by appropriately increasing the width of the single channel.

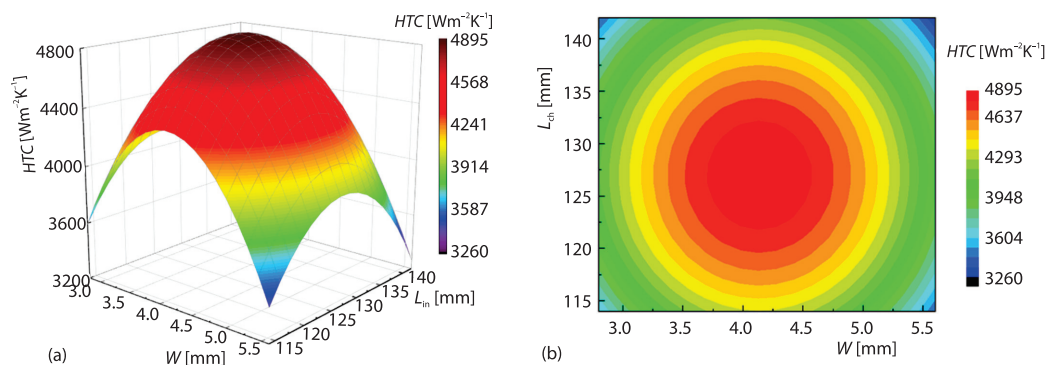


Figure 13. Effect of the channel length and single channel width on HTC; (a) 3-D curved surface diagram and (b) 2-D isogram diagram

Analysis of the contribution rate of the parameters

The variance contribution rate of different optimization variables to the optimization target was compared by analysis of variance (ANOVA) [33], which can quantify the signifi-

cance of the influence of each optimization variable on the target, so as to obtain the ranking of the influence degree of each parameter on each optimization target. As shown in fig. 14, the W accounts for the largest proportion of the contribution rates of the S , P_{total} , and HTC, which are 90.09, 76.99, and 72.24%, respectively. These findings indicate that the width of a single channel is a structural parameter that plays a key role in the flow of the heat exchange medium and the heat exchange process in the heat exchanger cavity. At the same time, the results also reveal that the L_{ch} of the parallel flow channel is a secondary factor affecting the flow and heat transfer process, the impact of the L_{ch} on the P_{total} is less than that of the remaining optimization goals, with a variance contribution rate of 5.11%. However, the impact on the HTC is greater than that of the remaining optimization goals, with a variance contribution rate of 14.18%. In addition, the effect of the structural parameters L_{in} and L_{out} in the mainstream area on the optimization goal is less pronounced than the flow channel parameters W and L_{ch} . Compared with the influence of the parameters in the mainstream area, the variance contribution rate of the L_{in} to each optimization goal is higher than that of the L_{out} . This suggests that when considering the optimization of the structure of the mainstream area to improve the optimization goal, more attention should be paid to the influence of the structure change of the inlet mainstream area on the flow and heat transfer process of the heat exchange medium.

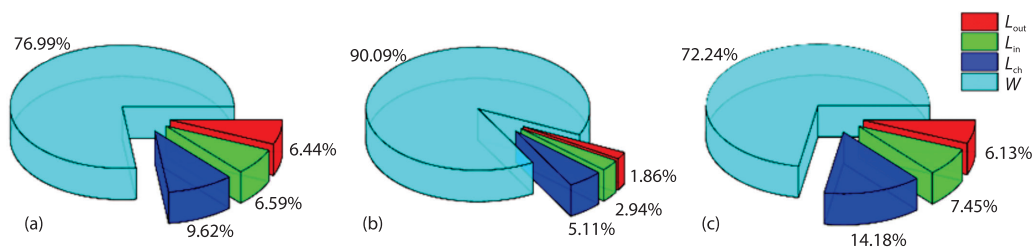


Figure 14. Contribution rate of different optimization variables to each optimization goal; (a) S , (b) P_{total} and (c) HTC

Analysis of multi-objective optimization results via NSGA-II algorithm

The optimal solution of the objective function is searched using the NSGA-II algorithm implemented in the iSIGHT software. The NSGA-II algorithm was proposed by Deb *et al.* [34] and is an improved algorithm based on the genetic algorithm. After the optimization algorithm is completed, several solutions belonging to the Pareto solution set are obtained. At this time, it is necessary to select the most satisfactory optimization plan from the Pareto solution set according to the actual situation [35]. The leading edge of the 3-D Pareto solution set obtained by the NSGA-II algorithm is shown in fig. 15.

The optimization scheme and its optimization target response value determined after comparing the optimization target results of each scheme in the Pareto solution set, are shown in tab. 7. The results reveal that the re-

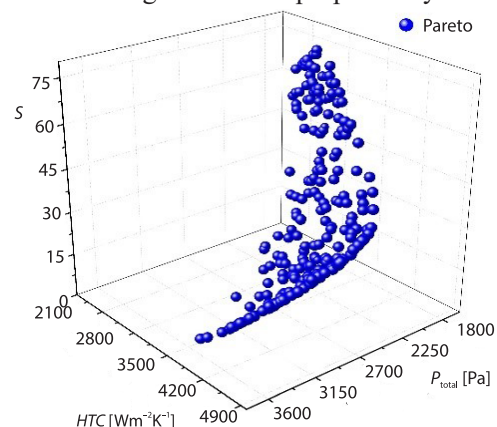


Figure 15. The 3-D Pareto solution frontiers

response value derived from the response surface model and the simulation result derived from the numerical simulation have a relatively high degree of agreement. The errors in the S , P_{total} , and HTC are 0.46, 2.68, and 1.51%, respectively, and the optimal results are reasonable. After multi-objective optimization design of the cavity structure parameters, the S , P_{total} , and HTC were significantly improved. The S and P_{total} decreased by 53.49 and 19.52%, respectively, while the HTC increased by 28.05%.

Table 7. Verification and comparison of the optimization results

Factors	Original model	Optimization results			Improvement [%]
		Optimal solution model	Simulation verification model	Response value error [%]	
L_{in} [mm]	83.5	85.5	85.5	–	–
L_{out} [mm]	59	70.3	70.3	–	–
L_{ch} [mm]	138	129.1	129.1	–	–
W [mm]	2.8	3.8	3.8	–	–
Evaluation index					
S	42.43	19.72	19.81	0.46	-53.49
P_{total} [Pa]	3893.35	3133.61	3217.62	2.68	-19.52
HTC [$\text{Wm}^{-2}\text{K}^{-1}$]	3105.12	4037.13	3976.58	1.51	+28.05

Conclusions

In this paper, the Latin hypercube sampling method and the response surface approximation model method are used to establish a response surface model with the L_{in} , L_{out} , W , and L_{ch} as independent variables, and the S , P_{total} , and HTC as the dependent variables. The influence of each structural parameter and the coupling effect of the parameters on the evaluation index is analyzed, and the optimal structural model is derived based on the NSGA-II algorithm.

- Based on the established response surface model, the degree of influence of each structural parameter on the evaluation index is determined by combining the variance contribution rate. The results show that the W is the primary structural parameter that affects the evaluation index. As the W increases, the S increases slowly at first and then abruptly, the P_{total} gradually decreases, and the HTC shows an increasing trend at first and then decreases. The L_{ch} is a secondary structural parameter that affects the evaluation index. The importance of the structural parameters of the parallel flow channel is clearly greater than that of the mainstream area.
- The focus of the parallel flow channel design in the HVH system is to find an appropriate balance between the enhancement of heat transfer and the reduction of the S and P_{total} to find the best solution. When the structural parameters are $L_{\text{in}} = 85.5$ mm, $L_{\text{out}} = 70.3$ mm, $L_{\text{ch}} = 121.9$ mm, and $W = 3.8$ mm, the combination of these parameters is optimal.
- The optimization goal of the most satisfactory optimization plan has been significantly improved, and the ideal results are achieved through a multi-objective optimization design. The results showed that the S and P_{total} decreased by 53.49% and 19.52%, respectively, while HTC increased by 28.05%.

Acknowledgment

This work was funded by Projects of *Six talent peak* of Jiangsu Province [Grant No. 2017-JSQC-008], Postgraduate Research & Practice Innovation Program of Jiangsu Province [Grant No. SJCX19_1150].

Nomenclature

C_p – specific heat at constant pressure, [$\text{Jkg}^{-1}\text{K}^{-1}$]	W – single channel width, [m]
HTC – average heat transfer coefficient, [$\text{Wm}^{-2}\text{K}^{-1}$]	<i>Greek symbols</i>
k – turbulent kinetic energy	β_0 – regression constant
L_{ch} – length of the parallel flow channel, [m]	β_j – linear coefficient
L_{in} – length of the mainstream area of the inlet, [m]	β_{ij} – co-ordinate coefficient
L_{out} – length of the mainstream area of the outlet, [m]	β_{ij} – square coefficient
S – flow distribution uniformity coefficient	ε_0 – the random error
P_{total} – inlet/outlet pressure drop, [Pa]	κ_p – heat transfer coefficient, [$\text{Wm}^{-2}\text{K}^{-1}$]
q_i – flow rate in the i^{th} flow channel, [ms^{-1}]	μ – viscosity, [$\text{mPa}\cdot\text{s}$]
\bar{q} – average flow rate of all flow channels, [ms^{-1}]	ρ – density, [kgm^{-3}]
T_{in} – inlet temperature, [$^{\circ}\text{C}$]	ω – specific dissipation rate
T_{mid} – intermediate runner temperature, [$^{\circ}\text{C}$]	
T_{out} – output temperature, [$^{\circ}\text{C}$]	

References

- [1] Alipanah, M., Li, X., Numerical Studies of Lithium-Ion Battery Thermal Management Systems Using Phase Change Materials and Metal Foams, *International Journal of Heat and Mass Transfer*, 102 (2016), Nov., pp. 1159-1168
- [2] Liu, H. L., et al., The Performance Management of a Li-Ion Battery by Using Tree-Like Mini-Channel Heat Sinks: Experimental and Numerical Optimization, *Energy*, 189 (2019), 1, pp. 116150.1-116150.15
- [3] Feng, X., Hu, J., Analysis and Optimization Control of Finned Heat Dissipation Performance for Automobile Power Lithium Battery Pack, *Thermal Science*, 24 (2020), 5B, pp. 3405-3412
- [4] Wang, R. J., et al., Study on Dynamic Thermal Control Performance of Positive Temperature Coefficient (PTC) Material Based on a Novel Heat Transfer Model Considering Internal Heat Transfer, *Applied Thermal Engineering*, 165 (2020), 114452
- [5] Kim, K. Y., et al., Experimental Studies on the Heating Performance of the PTC Heater and Heat Pump Combined System in Fuel Cells and Electric Vehicles, *International Journal of Automotive Technology*, 13 (2012), 6, pp. 971-977
- [6] Yoon, S., et al., Performance Characteristics of a Modularized and Integrated PTC Heating System for an Electric Vehicle, *Energie*, 9 (2016), 1, pp. 3821-3838
- [7] Lee, D., et al., Performance Characteristics of Mobile Heat Pump for a Large Passenger Electric Vehicle, *Applied Thermal Engineering*, 50 (2013), 1, pp. 660-669
- [8] Jamil, S. R., et al., Techno-Economic Analysis of a Novel Hybrid Heat Pump System to Recover Waste Heat and Condensate from the Low-Temperature Boiler Exhaust Gas, *International Journal of Energy Research*, 44 (2020), 5, pp. 3821-3838
- [9] Ishaque, S., et al., Effect of Heat Exchanger Design on Seasonal Performance of Heat Pump Systems, *International Journal of Heat and Mass Transfer*, 151 (2020), 119404
- [10] Hainzmaier, C., et al., New Methods of Heating Hybrid and Electric Vehicles, SAE paper, 2015-01-1711, 2015
- [11] Alneama, A., et al., An Experimental and Numerical Investigation of the Use of Liquid-flow in Serpentine Micro-channels for Microelectronics Cooling, *Applied Thermal Engineerin*, 116 (2017), Apr., pp. 709-723
- [12] Rostami, L., et al., A Numerical Investigation of Serpentine Flow Channel with Different Bend Sizes in Polymer Electrolyte Membrane Fuel Cells, *Energy*, 97 (2016), Feb., pp. 400-410
- [13] Dong, F., et al., Effects on Thermal Performance Enhancement of Pin-Fin Structures for Insulated Gate Bipolar Transistor (IGBT) Cooling in High Voltage Heater System, *International Journal of Thermal Sciences*, 146 (2019), 106106
- [14] Shian, L., Sunden, B., Numerical Study on Thermal Performance of Non-Uniform Flow Channel Designs for Cooling Plates of PEM Fuel Cells, *Numerical Heat Transfer, Part A*, 74 (2018), 1, pp. 917-930

- [15] Li, Y., Shen, et al., Heat Transfer Enhancement of Rotating Wedge-Shaped Channels with Pin Fins and Kagome Lattices, *Numerical Heat Transfer, Part A*, 77 (2020), 12, pp. 1014-1033
- [16] Li, J., Peterson, G., The 3-Dimensional Numerical Optimization of Silicon-based High Performance Parallel Micro-channel Heat Sink with Liquid-flow, *International Journal of Heat & Mass Transfer*, 50 (2007), 15-16, pp. 2895-2904
- [17] Zhang, W., et al., Analysis and Optimization of Flow Distribution in Parallel-Channel Configurations for Proton Exchange Membrane Fuel Cells, *Journal of Power Sources*, 192 (2009), 2, pp. 931-940
- [18] Cao, X., et al. Thermal Performance of Double Serpentine Minichannel Heat Sinks: Effects of Inlet-Outlet Arrangements and through-Holes, *International Journal of Heat and Mass Transfer*, 153 (2020), 119575
- [19] Cao, X., et al., Heat Transfer Performance of a Novel Multi-Baffle-Type Heat Sink. Entropy, *Entropy*, 20 (2018), 979
- [20] Ahmed, A. I., et al., Numerical and Experimental Investigation of Heat Transfer in Liquid Cooling Serpentine Mini-Channel Heat Sink with Different New Configuration Models, *Thermal Science and Engineering Progress*, 6 (2018), June, pp. 128-139
- [21] Maharudrayya, S., et al., Flow Distribution and Pressure Drop in Parallel-Channel Configurations of Planar Fuel Cells, *Power Sources*, 144 (2005), 1, pp. 94-106
- [22] Huang, W., Zhu, Q., Flow Distribution in U-type Layers or Stacks of Planar Fuel Cells, *Journal Power Sources*, 178 (2008), 1, pp. 353-362
- [23] Liu, H. L., et al., Heat Transfer and Flow Performance of a Novel T-type Heat Sink with GaInSn Coolant, *International Journal of Thermal Sciences*, 144 (2019), Oct., pp. 129-146
- [24] Liu, H. L., et al., Heat Transfer Performance of T-Y Type Micro-Channel Heat Sink with Liquid GaInSn Coolant, *International Journal of Thermal Sciences*, 120 (2017), Oct., pp. 203-219
- [25] Biswal, L., et al., Design and Optimization of Single-Phase Liquid Cooled Micro-Channel Heat Sink, *IEEE Transactions on Components & Packaging Technologies*. 32 (2010), 4, pp. 876-886
- [26] Wang, J., Pressure Drop and Flow Distribution in Parallel-Channel Configurations of Fuel Cells: U-type Arrangement, *International Journal of Hydrogen Energy*, 33 (2008), 21, pp. 6339-6350
- [27] Wang, J., Pressure Drop and Flow Distribution in Parallel-channel Configurations of Fuel Cells: Z-type Arrangement, *International Journal of Hydrogen Energy*, 35 (2010), 11, pp. 5489-5509
- [28] Tong, J., et al., Geometric Strategies for Attainment of Identical Outflows through all of the Exit Ports of a Distribution Manifold in a Manifold System, *Applied Thermal Engineerin*, 29 (2009), 17, pp. 3552-3560
- [29] Ghozatloo, A., et al., Convective Heat Transfer Enhancement of Graphene Nanofluids in Shell and Tube Heat Exchanger, *Experimental Thermal & Fluid Science*, 53 (2014), 2, pp. 136-141
- [30] Rakhimov, A. C., et al., Uncertainty Quantification Method for CFD Validated for Turbulent Mixing Experiments from GEMIX, *Nuclear Engineering and Design*, 358 (2020), Mar., pp. 110444.1-110444.8.
- [31] Ganapathy, T., et al., Optimization of Performance Parameters of Diesel Engine with Jatropha Biodiesel Using Response Surface Methodology, *International Journal of Solar Energy*, 30 (2011), Suppl. 1, pp. 76-90
- [32] Park, J., et al., A Study on Flow Characteristics and Flow Uniformity for the Efficient Design of a Flow Frame in a Redox Flow Battery, *Applied Sciences*, 10 (2020), 3, 929
- [33] Jeong, S., et al., Data Mining for Aerodynamic Design Space, *Journal of Aerospace Computing Information & Communication*, 2 (2005), 11, pp. 452-162
- [34] Deb, K., et al., A Fast Elitist Non-Dominated Sorting Genetic Algorithm for Multi-Objective Optimization: NSGA-II, *Parallel Problem Solving from Nature PPSN VI. 1917*, (eds. Schoenauer, M., et al.) Springer, Verlag, Berlin, 2000, Vol. 1917, pp. 849-858
- [35] Yang, K., et al., Multi-Objective Steady-State Optimization of Two-Chamber Microbial Fuel Cells, *Chinese Journal of Chemical Engineering*, 25 (2017), 8, pp. 1000-1012